Journal of Fluorine Chemistry 231 (2020) 109457

Contents lists available at ScienceDirect

Journal of Fluorine Chemistry

journal homepage: www.elsevier.com/locate/fluor

Multimodal upconversion CaF_2:Mn/Yb/Er/Si nanoparticles

V.G. Ilves[a,*], S.Y. Sokovnin[a,b], M.G. Zuev[b,c], M.A. Uimin[d], D.V. Privalova[d], J. Kozlova[e], V. Sammelselg[e,f]

[a] Institute of Electrophysics Ural Branch RAS, Yekaterinburg, 620016, Russia
[b] Ural Federal University, Yekaterinburg, 620002, Russia
[c] Institute of Solid State Chemistry Ural Branch RAS, Yekaterinburg, 620990, Russia
[d] Miheev Institute of Metal Physics Ural Branch RAS, Yekaterinburg, 620018, Russia
[e] Institute of Physics, University of Tartu, Tartu, 50411, Estonia
[f] Institute of Chemistry, University of Tartu, Tartu, 50411, Estonia

ARTICLE INFO

Keywords:
Upconversion NPs
Multimodal NPs
Mesoporous NPs
Paramagnetic NPs

ABSTRACT

The mesoporous nanocrystalline CaF_2:Mn/Yb/Er/Si powder was obtained by pulsed electron beam evaporation (PEBE) method in a vacuum. The specific surface area (SSA) of the nanopowder (NP) reached a value of 296 m^2/g. The effect of thermal annealing in the air on the structural, textural, thermal, magnetic, and luminescent properties of CaF_2:Mn/Yb/Er/Si NPs has been studied. The NPs have demonstrated the dominant RED-NIR upconversion (UC) luminescence under the exposure to the 980-nm laser radiation. The paramagnetic properties of CaF_2:Mn/Yb/Er /Si NPs suggest the possibility of their use in magnetic resonance (MR) imaging. The annealing of NPs in the air has confirmed their high thermal stability in the temperature range from the room temperature (RT) to 400 °C. The developed NPs have a potential for the use as a trimodal agent in UC/MR/CT imaging in nanomedicine.

1. Introduction

The progress achieved in the field of nanotechnologies and nanomaterials stimulates the development of functional nanoparticles (NPs) as bio-probes for various biomedical applications [1]. Unimodal NPs with optical or magnetic characteristics are widely used in bio-probing and bio-imaging. Nevertheless, they do not allow obtaining all the needed information about biological samples [2]. Requirements of up-to-date biomedical technology assume development of new-generation multimodal bio-probes. Multimodal biomarkers combining two or more functions become a new challenge in biology and medicine [3]. In particular, inorganic NPs doped with trivalent ions of rare-earth elements (REE) have unique electronic structures and unusual optical and magnetic properties, and they are promising candidates for multimodal bio-applications [4]. Usually, a crystal matrix is doped with REE ions and /or transition metal (TM) ions as luminescent centers [5]. Outstanding properties of NPs doped with REE ions, such as narrow width of f-f emission bands, long fluorescence lifetime, near-infrared (NIR) excitation, large anti-Stokes shifts for considerable separation of upconversion luminescence (UCL) from excitation, weak anti-fluorescent background with the high signal-to-noise ratio, low cytotoxicity, high chemical stability, and high resistance to photobleaching, make them very suitable for using in various bio-applications as an alternative to organic fluorescent dyes, carbon nanotubes, and quantum dots [5,6].

In particular, in upconversion nanoparticles (UCNP) the emission and excitation wavelengths can fall within the bio-tissue transmission window covering approximately the wavelength range from 700 to 1000 nm, which makes UCNP suitable for deep imaging of tissues [7,8]. However, traditional lanthanide activators, such as Tm^{3+} and Er^{3+} ions, have many metastable excited states. Therefore, the dominant emission band often lies beyond the red spectral range with the relatively low red emission intensity [9]. That is why the strategy of increasing the red emission intensity is used more and more often for different UC applications, especially, for deep imaging of tissues [5,10]. It should be noted that the intensity of emission in the NIR 800-nm band is much higher than the emission of any other band. This fact indicates the high potential of the above strategy for deep imaging of tissues [11,12].

Today, the 3D reconstruction of a unimodal medical image (magnetic resonance imaging (MRI), computer tomography (CT), positron emission tomography (PET), single-photon emission computer tomography (SPECT), and optical imaging can give a bright image of tissues, but fails to provide accurate and thorough information for clinical practice. Therefore, various bimodal, trimodal, and even four-modal

---

* Corresponding author.
E-mail address: ilves@iep.uran.ru (V.G. Ilves).

https://doi.org/10.1016/j.jfluchem.2020.109457
Received 7 October 2019; Received in revised form 19 December 2019; Accepted 19 December 2019

imaging technologies [13], such as, for example, UCPL/MR/CT [14], UCPL/MR/PET [15], and UCPL/CT/MR/SPECT [16] attract significant attention. It is believed that the combination of different methods of molecular imaging in multifunctional NPs can compensate for disadvantages of the methods, in particular, in respect of the spatial resolution, penetration depth, and so on.

The optical properties of REE- and TM-doped luminescent NPs depend strongly on the crystal lattice of the matrix, they reside in [17]. The photoluminescence (PL) lifetime and the PL efficiency of dopants depend significantly on the structure, local symmetry, strength of the crystal field, and energy of matrix phonons [18].

Fluorides, owing to their high chemical stability and low phonon energy ($< 350\ cm^{-1}$ [19]), are considered as the most efficient materials for doping with lanthanides (Ln^{3+}) in order to achieve the desired luminescence (UCPL or Stokes luminescence). Among fluoride NPs doped with lanthanides, calcium fluoride is characterized by the best bio-compatibility [20].

The synthesis of high-emission CaF_2: Ln^{3+} NPs is now a problem because of the effect of surface quenching [21]. In addition, it is hard to control the morphology of CaF_2 NPs at heterovalent doping with Ln^{3+} ions in different concentrations [22]. That is why the development of an efficient strategy for the preparation of CaF_2: Ln^{3+} NPs with intense PL and different concentration of dopant Ln^{3+} ions for various bio-applications is an urgent problem. The number of studies dealing with the synthesis of fluoride UCNPs doped with REE ions and Mn ions for the further use as multimodal contrast agents [23] in theranostics of cancer cells [24] and deep imaging of tissues [25] has increased considerably in the last decade. The luminescent $NaYF_4$ matrix is believed to be the most efficient among fluorides [26], but it is more toxic in comparison with CaF_2 [16]. That is why calcium fluoride as a matrix is interesting for the synthesis of multimodal UCNPs. The paramagnetic Mn^{2+} ion was introduced into the CaF_2 matrix to add the MRI mode [27] and to intensify the red band of luminescence. Now there are only few data on NPs based on CaF_2 with high longitudinal relaxivity for MRI [28–31].

The objective of this paper was the synthesis using the method of pulsed electron-beam evaporation (PEBE) in a vacuum [32] and the study of physical-chemical characteristics of multimodal CaF_2:Mn/Yb/Er/Si nanopowder promising for use in nanomedicine, dosimetry, and photonics. The effect of changes in the concentration of manganese fluoride and thermal annealing of the CaF_2:Mn/Yb/Er/Si nanopowder on the structure, magnetic, relaxation, and luminescent properties of the samples has been studied.

2. Experimental

2.1. Justification of choice of the target composition

To meet biolabeling requirements, UCNPs should have the high dispersibility in water [33,34], good bio-compatibility, nanometer size of 30–100 nm, high luminescent intensity [35], the feasibility of functionalization of the nanoparticle surface, minimal toxicity, high stability and photostability, and easy elimination from the human body [36].

When choosing the target composition to obtain a multimodal UCPL/MR/CT contrast agent (CA), we based upon the following requirements to CA:

(I) dopants and the matrix should have minimal toxicity. Therefore, in place of the toxic Gd^{3+} ion widely used in contrast agents for magnetic resonance imaging (MRI) [37], we selected for Mn. The Mn^{2+} ion has paramagnetic properties at the room temperature, which favors the creation of CA for MRI [37]. Manganese and calcium are naturally present in the human body. Thus, they determine the low toxicity of the multimodal material. CaF_2 is more bio-compatible in comparison with the most promising modern up-conversion material – $NaYF_4$ doped with a couple of rare-earth Yb^{3+} and Er^{3+} ions [38,39];

(II) among fluorides of alkali-earth metals (MF_2, M = Ca, Ba, and Sr) for creation of the multimodal material based on the MF_2-MnF_2 system, CaF_2 is most suitable by the following reasons:

a) it is well-known [40] that the matrix based on the CaF_2-Mn system luminesces in the blue spectral range (λ_{max} = 490 nm), whereas the doping of BaF_2 and SrF_2 fluorides with Mn^{2+} ions leads to suppression of photoluminescence in the temperature range from 10 to 200 K [41].

b) The CaF_2-MnF_2 phase diagram is studied quite thoroughly [42]. The wide range of MnF_2 solubility in the CaF_2 lattice allows the matrix to be doped with manganese in a wide range of concentrations (up to 47 mol.%). The solubility of rare-earth elements (REEs) (in this case, Yb and Er ions) in CaF_2 is also rather high [43–45].

d) The matrix and dopants should have a minimal cost. Among fluorides of alkali-earth metals, the CaF_2 matrix meets this requirement. The easiest way to dope the CaF_2 matrix is to use RE trifluorides since the solid-state solutions of fluorite type like $M_{1-x}R_xF_{2+x}$ (M = Ca, Sr, Ba, R – RRE) exist in all MF_2-RF_3 systems [46]. However, the cost of RE trifluorides is an order of magnitude higher than that of RE oxides. That is why we selected the latter as dopants, despite the injection of RE oxides into the target could lead to an undesirable increase of the oxygen concentration in the end product.

(III) To give upconversion to the Mn- CaF_2 matrix, we have selected the Yb–Er couple among the most widely used donor-acceptor couples (Yb–Er, Yb–Tm, Yb–Ho). The choice was determined by the fact that apart from the efficient energy transfer from Yb to Er allowing NIR-to-VIS upconversion, the visible luminescence of Er^{3+} ions lies in the spectral range, where commercial multiphoton microscopes have the highest detection response [47].

(IV) To increase the porosity and hydrophilicity and to decrease the toxicity of the end product at the expense of a silica shell created (due to the self-organization effect) on the surface of synthesized NPs, cheap Aerosil-90 NPs (Degussa, Germany) were added to the target composition. When Aerosil (90) is used, it becomes unnecessary using expensive mesoporous nanopowders like MSM-41 or SB-15 [48]. The earlier studies of the porosity of silicate [49], pure fluoride BaF_2 [50], and oxide [51] nanopowders have shown that mesoporous nanopowders consisting of nonporous NPs with developed interparticle porosity are formed if the PEBE method is used [52]. The closed analogs are nanopowders of different Aerosils obtained by the method of flame synthesis [53]. However, generation of multicomponent NPs with the application of the flame synthesis method is somewhat more difficult in comparison with PEBE in view of the difficult selection of initial precursors.

Based on the foregoing reasons, for tentative analysis, we have selected the CaF_2 fluoride as a matrix and MnF_2 fluoride and Yb_2O_3, Er_2O_3, and SiO_2 oxides as dopants.

2.2. Experimental

The CaF2:Mn/Yb/Er/Si NPs were obtained with the PEBE in vacuum at the NANOBEAM-2 setup [54] (residual pressure of 4 Pa).

The targets to be evaporated were made from micron-sized powders: CaF_2 calcium fluoride (ultra-high purity, TU 6-09-2412-84, SSA = 18.47 m^2/ g), water manganese fluoride MnF_2*nH_2O (high purity, TU 6-09-01-367-76), Yb_2O_3 (99.99 %, China), Er_2O_3 (99.99 %, China), and Aerosil90 SiO_2 NP (Degussa, Germany). Prior to mixing, the MnF_2*nH_2O powder was dried in air at the temperature of 120 °C for 1 h. The target components were mixed manually in an alundum crucible and pressed at a PRG-1 press at a pressure of 50 kN into the tablet with the diameter of 40 mm and the height of 10 – 15 mm. To improve the density of the tablets, about 5 mm^3 of isopropyl alcohol was added to the mechanic mixture. The obtained tablets were not annealed in the air to avoid adding extra oxygen in calcium fluoride during annealing. Then the target was kept in a vacuum for 24 h and subjected to direct evaporation. The concentrations of the target components are given in Table 1.

Table 1
Concentrations of initial components of the target.

Components	Wt.%
CaF_2	86.0
MnF_2	4.5
Yb_2O_3	4.3
Er_2O_3	0.4
SiO_2	4.8

The following operating conditions of the Nanobeam-2 setup were used: accelerating voltage of 40 kV, beam current of 0.2 A, the pulse duration of 100 μs, pulse repetition frequency of 100 Hz, beam sweep on the target of 2.5 cm^2, and evaporation time of 50 min. NPs were deposited onto large-area window-glass substrates separated by 10 − 15 cm from the target center. The following isothermal annealing of CaF_2:Mn/Yb/Er/Si NPs was conducted in alundum crucibles in the air at a temperature of 200, 400, 600, and 900 °C for 10 min. From here on in this paper, CaF_2:Mn/Yb/Er/Si samples as-prepared and annealed at the temperature of 200, 400, and 900 °C were designated as S0, S200, S400, S600, and S900, respectively.

For analysis of NP properties, the following diagnostics were used. The SSA of powders was determined by the Brunauer-Emmet-Taylor (BET) method at the Micromeritics TriStar 3000 setup after degassing of the studied material in vacuum at the temperature of 100 °C for 1 h. The X-ray diffraction (XRD) analysis was carried out at the XRD 7000 Shimadzu diffractometer (Japan). The imaging of the samples was performed at the CuK*α*–radiation with a nickel filter in the 2θ angle range from 20 to 90°. The morphology of the CaF_2:Mn/Yb/Er/Si NPs was observed using the FEI Helios NanoLab 600 high-resolution scanning electron microscope (HRSEM). For SEM studies, nanoparticles were fixed on SEM stubs using double-sided carbon adhesive tape. SEM was also performed in the scanning transmission electron microscopy (STEM) mode. For the STEM mode, a drop of the nanoparticle solution in isopropanol was deposited on a copper grid coated with a carbon film. The elemental composition was characterized by an Oxford Instruments energy dispersive x-ray (EDX) spectrometer connected to the same microscope. Magnetization curves were recorded at the Faraday balance (sensitivity of 10^{-5} emu/g). The thermal analysis of nanopowders with the thermogravimetric (TG) and differential scanning calorimetry (DSC) methods was carried out at the STA-409-PC Luxx synchronous thermoanalyzer combined with the QMS-403C mass-spectrometer (NETZSCH). Upconversion spectra were recorded at the MDR-204 spectrometer (Hamamatsu R928 photoelectronic multiplier tube) under the excitation by the KLM-H980-200-5 laser unit (wavelength of 982 ± 5 nm, power of 221 mW). The entrance and exit slits of the monochromator were 1.2 mm.

3. Results and discussion

3.1. XRD

XRD measurement was used to determine the phase composition of the as-prepared samples. As shown in Fig. 1(a), the S0, S220 and S400 samples had the single-phase structure, and the diffraction peaks are in agreement with the ordered cubic structure of CaF_2 (JCPDS file No. 00-035-0816) [55]. The peaks at the angles 2θ = 28.2674, 47.0203, 55.7784 and 68.6680 correspond to the indices < h k l > of (1 1 1), (2 2 0), (3 1 1), and (4 0 0), respectively [56,57].

In the X-ray pattern of the S900 sample, one can see peaks of the secondary phases (Fig.1b). The peaks of the CaF_2 phase in the X-ray pattern of the S900 sample are much narrower than the corresponding peaks of all other samples, which is indicative of the high crystallinity and large grain size.

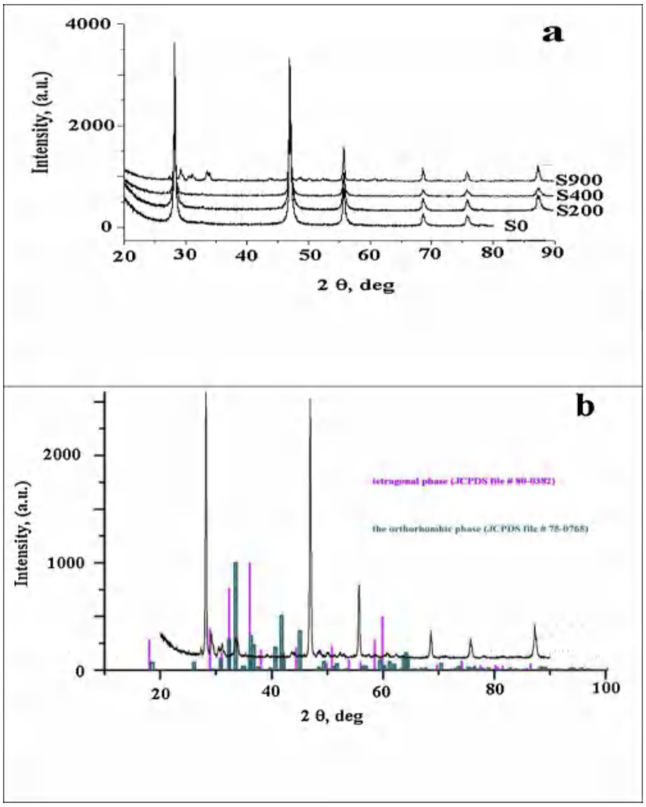

Fig. 1. a) Diffractograms of S0, S200, S400, and S900 samples; **b)** Diffractogram of S900 sample and reference lines of tetragonal (JCPDS No. 01-080-0382 (pink) and orthorhombic (JCPDS No. 075-0765 (green)) phases of manganese oxides.

Table 2
Lattice parameters in CaF2:Mn/Yb/Er/Si nanoparticle samples.

Sample	Lattice parameter***a***, Å
S0	5.4693 (5)
S200	5.4686 (9)
S400	5.4697 (11)
S900	5.4699 (9)
CaF_2 (PEBE)	5.4624; 5.463(1) [58]
CaF^2: Er^{3+}:Yb^{3+} = 0.78 : 0.20 : 0.02 [58]	5.469(2) [58]
CaF_2	5.4606 (6)

The dimensions of a unit cell in all the samples are identical within the uncertainty (Table 2).

The lattice parameters of NPs in Table 2 are in a good agreement with the lattice parameters of CaF_2:Yb/Er NPs (CaF_2: Er^{3+}:Yb^{3+} = 0.78:0.20:0.02 nominal molar ratio) in [58]. We also observed an increase of the lattice parameters of CaF2:Mn/Yb/Er/Si NP in comparison with the lattice parameter of pure CaF_2 obtained by the PEBE method (Table 2). This increase is caused by the electron repulsion between fluorine ions distributed not only in fluoride lattice nodes, but also in interstices [59].

Additional diffraction peaks from impurity phases are clearly seen in the diffractogram of the S900 sample. In the study of the effect of annealing on nanocrystal Mn-doped CaF_2 powders [60], the impurity phases (Mn_3O_4 and MnO_2) formed after the annealing at the temperature of 800 °C were found in the X-ray pattern of the CaF_2:Mn sample (3.0 mol%). The impurity phases formed as a result of the diffusion of atmospheric oxygen at the sample annealing. The assignment of x-ray patterns has shown the presence of tetragonal and orthorombic phases of Mn_3O_4 spinel, whose structure includes Mn^{2+} ions in the tetrahedral coordination and Mn^{3+} ions of the octahedral coordination, respectively. During the annealing of samples in [60], the sample color

Table 3
Results of elemental analysis (at %) of CaF_2:Mn/Yb/Er/Si NPs by the EDX method.

Sample	The concentration of elements in the samples, at.%*								
	C	O	F	Si	Ca	Mn	Er	Yb	Total
S0	21.3	4.7	52.8	1.1	16.5	3.3	0.03	0.3	100.00
S200	4.8	3.7	62.3	1.1	23.2	4.6	0.03	0.3	100.00
S400	14.4	6.2	53.8	1.2	20.2	4.0	0.01	0.3	100.00
Std. deviation	11.40	1.67	7.97	0.42	4.65	1.25	0.06	0.08	

* Average element concentrations determined at different parts of every sample are given.

changed gradually from white to dark brown as the sample temperature achieved 800 °C (Fig. S2a). The smooth change in the color of our samples during the annealing from white (RT) to black (900 °C) (Fig. S2b) indicates visually the possible change in the valence of the Mn ion from 2+ to 4+ (MnO_2 (IV) oxide has the pronounced black color). The assignment of the diffractogram of the S900 sample (Fig. 1b) has shown the presence of tetragonal MnO_2 (JCPDS file № 80-0382) and orthogonal Mn_2O_3 (JCPDS file № 75-076) impurity phases in the S900 sample, which is in agreement with the results reported in [60].

3.2. Energy dispersive X-ray microanalysis

Results of the elemental analysis (wt %) of CaF_2:Mn/Yb/Er/Si nanoparticle samples are given in Table 3. The presence of lanthanide ions in CaF_2:Mn/Yb/Er/Si NPs is confirmed by the data of the EDX spectrum (Fig. S1). In the EDX spectra, the peaks of Yb, Mn, and Si are clearly seen, while the peaks assigned to Er^{3+} ions at some parts of the S0, S200, and S400 samples practically are not observed because of the low ion concentration, which is lower than the EDX detection threshold. On the other hand, the presence of Er^{3+} ions is confirmed by their typical emission peaks, which will be demonstrated below in the upconversion spectra under the excitation by the 980-nm laser and in the cathodoluminescence spectra excited by a pulsed electron beam with the electron energy of 180 keV.

It follows from Table 3 that the concentration of fluorine ions in the CaF_2 matrix lattice far exceeds the stoichiometric ratio Ca:F = 1:2. This confirms the above idea on the growth of the lattice parameter in doped samples at the expense of interstitial fluorine ions. The increased Mn concentration in NPs was quite expected because of the high pressure of the MnF_2 vapor in comparison with the vapors of all other components.

The high content of foreign carbon in the as-prepared S0 sample is connected with the conditions of synthesis of NPs (vapor of vacuum pump oil), whereas in the annealed S400 sample it is connected with adsorption of NPs from the environment during the annealing. The minimal concentration of carbon and oxygen impurities in the S200 sample indicates that the annealing temperature of 200 °C is optimal for removal of admixtures from mesoporous CaF_2:Mn/Yb/Er/Si NPs without a marked increase in the size of initial NPs. There is a possibility of impurity carbon resulting from isopropyl alcohol, which was used to compress the target.

In addition, the mapping has shown (Fig. S3) a slight nonuniformity in the distribution of SiO_2, whereas the other elements are distributed quite uniformly. Thus, we failed to detect the effect of clusterization with SE.

3.3. SEM analysis

SEM images of CaF_2:Mn/Yb/Er/Si NPs before and after annealing at the temperature of 200 and 400 °C are shown in Fig. 2.Initial (as-prepared) non-annealed CaF_2:Mn/Yb/Er/Si NPs were strongly agglomerated and had an irregular shape (Fig. 2a, b, c) typical of the most nonmetal NPs generated by the PEBE method [52]. Agglomerates of CaF_2:Mn/Yb/Er/Si NPs before and after annealing looked like spongy 3D structures (Fig. 2a, e, g) very similar to three-dimensional cross-linking silica networks (see Fig. 2a in [61]).

In addition, the non-annealed S0 sample (Fig. 2e) included some spherical micron-sized particles from 1 to 3 μm in size, which could be removed, whenever necessary, from the obtained nanopowder through sedimentation in a liquid medium with the prior ultrasonic processing. The change in morphology with an increase of the annealing temperature becomes marked only after annealing of NPs at the temperature of 400 °C. In the S400 sample (Fig. 2k), the number and the size of spherical particles are somewhat larger than those in the S0 and S200 samples (Fig. 2c, f), whose morphology is practically indistinguishable.

3.4. Textural properties of NPs

The adsorption-desorption isotherms and textural parameters of the S0, S200, S400, and S600 samples are shown in Fig. S4 and Table 4, respectively.

The isotherms of the IV type, which are typical for mesoporous materials, were observed in all the samples. The S0 and S200 samples showed the unimodal size distribution of the pores. To be noted are the high values of SSA and the pore volume in the S0, S200, and S600 samples.

The pore volume changes nonmonotonically as the annealing temperature increases: first, it decreases from 1.02 cm^3/g to 0.37 cm^3/g and then increases sharply up to 2.1 cm^3/g after annealing at the temperature of 600 °C. The leavening action, which leads to the sharp increase in the pore volume (2.1 cm^3/g) and specific surface up to 194 m^2/g in CaF_2-Mn/Yb/Er/Si NPs during the annealing in air at the temperature of 600 °C, is likely connected with the worse crystallinity of the CaF_2 matrix as a result of change in the valence of the Mn^{2+} ion to the Mn^{4+} ion at the consecutive phase transformation of manganese oxides by the following scheme: $MnO \rightarrow Mn_2O_3 \rightarrow Mn_3O_4$, which occurs on the surface of NPs during the annealing.

The combination of the uniform mesopore volume and small size of particles is quite favorable for drug load [62]. Such an important textural parameter as the pore volume (Vpore) is much larger in CaF_2-Mn/Yb/Er/Si NPs than, for example, in the popular upconversion $NaYF_4$:Yb,Er matrix [63], mesoporous CaF_2:Yb^{3+},Tm^{3+}@$mSiO_2$ nanospheres [64], ordered mesostructured LaF_3 nanoarrays [65]), and even well-ordered microscale MCM-41 mesoporous silica sheets [66] and SBA-15 [67].

3.5. DSC-TG analysis CaF_2-Mn/Yb/Er @SiO_2

Fig. 3 shows DSC-TG thermograms and mass-spectra of H_2O and CO_2 of the as-prepared S0 and annealed S400 samples during the heating in the air atmosphere up to the temperature of 1000 °C.

Fig. 3 depicts the thermograms of the S0 and S400 samples. The thermal analysis of the behavior of CaF_2-Mn/Yb/Er/Si/ NPs during the heating in the air with a rate of 10 deg/min up to 1000 °C has shown the following:

The loss of mass of the S0 and S400 samples at the heating up to 1000 °C was 4.1 and 1.0 %, respectively. The S0 sample lost about 2.5 % of mass for evaporation (section II in the TG curve, Fig. 3a) of carbonaceous compounds ($CaCO_3$, $Ca(OH)_2$ and others). The loss of mass

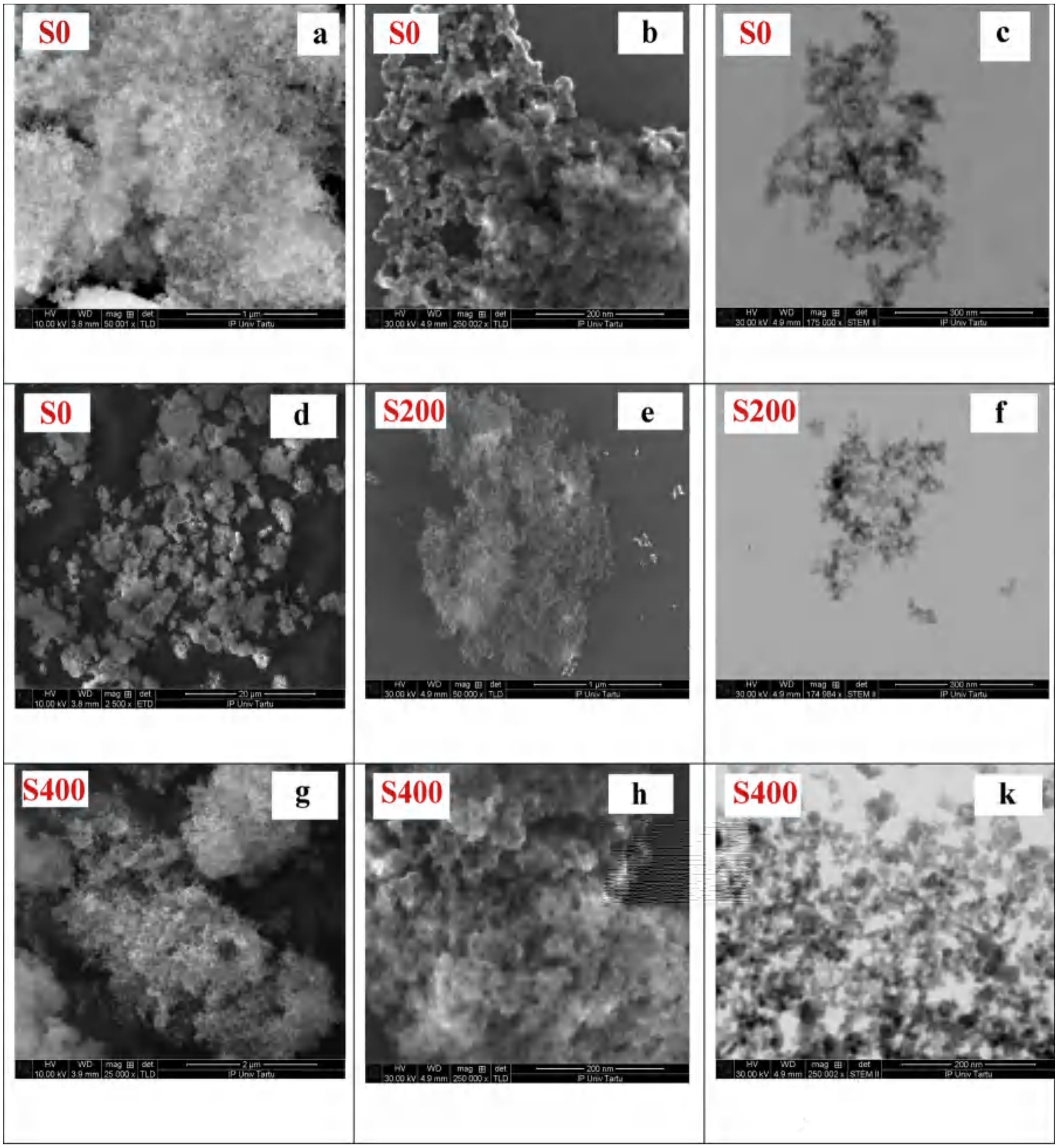

Fig. 2. SEM images of CaF_2:Mn/Yb/Er/Si NPs before and after annealing at the temperature of 200 and 400 °C in the ordinary (a,b,d,e,g,h) and transmission (c,f,k) modes.

Table 4

Texture parameters of the CaF_2:Mn /Yb /Er/Si before and after annealing.

Sample	SSA (m^2/g)	Pore volume (cm^3/g)	Pore size (nm)
S0	296 ± 2.8	1.02	32.3
S200	56.8 ± 2.5	0.48	23.5
S400	55 ± 0.7	0.37	29.9
S600	194 ± 5.0	2.10	29.8
NaYF4:Yb^{3+}/Er^{3+}@nSiO_2@mSiO_2 [63]	450	0.5	4.7
CaF_2:Yb^{3+},Tm^{3+}@mSiO_2 [64]	470	0,24	10,7
LaF_3 [65]	75	0,15	4
MSM-41 [66]	916.78	1.36	7.5
SBA-15 [67]	787	1.056	8.8

at section II of the TG curve was accompanied by a synchronous release of H_2O and CO_2 in the corresponding mass-spectral curves.

Two endothermal peaks were found in the DSC curve: the first peak in the temperature range 40180 ºC is caused by the evaporation of water adsorbed in mesopores and on the surface of NPs, the second peak in the temperature range ~780−875 °C may be a result of decomposition of calcium hydroxide and calcium carbonate in the following relations: $Ca(OH)_2 = CaO + H_2O$ (1) and $CaCO_3 = CaO + CO_2$ (2). The consecutive proceeding of the above decomposition reactions can be suggested from the structure of the peaks in the H_2O and CO_2 mass-spectra – each mass-spectrum includes two peaks, which appear synchronously at the heating and correspond to reactions (1) and (2). An insignificant loss of the sample mass at the heating from 780 to 1000 °C (less than 0.5 mass%) also confirms that the endothermal peak in the range ~780−875 °C corresponds to decomposition reactions (1) and (2) and desorption of interstitial atoms of excess fluorine, whose presence was indicated by the data of EDX analysis (strong non-stoichiometry at the expense of excess fluorine).

The thermal analysis of the S400 sample has shown (Fig. 3b) that the annealing at 400 °C has led to the practically absolute vanishing of

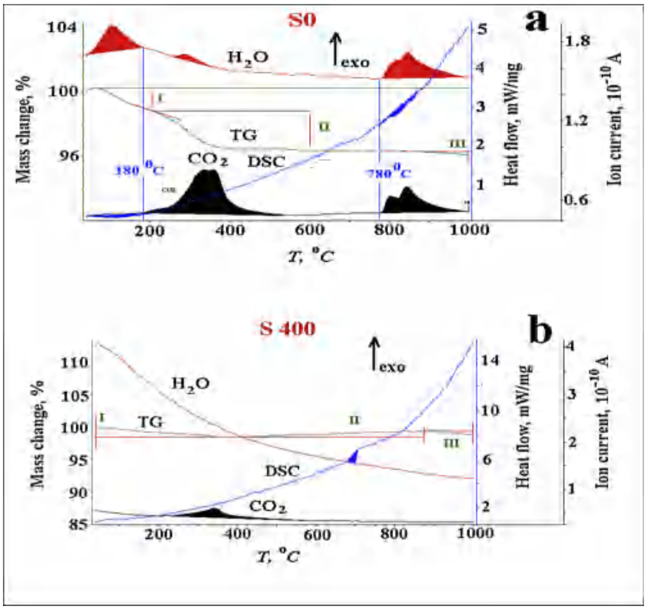

Fig. 3. Heating thermograms of synchronous DSC-TG analysis in the temperature range 40–1400 °C: a) S0 sample, b) S400 sample.

adsorbed water in the sample (O peaks are absent in the mass-spectral curve of water). Only one low-temperature peak associated with removal of residual carbonaceous compounds remained in the mass-spectral curve of CO_2. An insignificant loss of mass was observed up to the temperature of about 350 °C. Starting from 425 °C, the mass increased gradually due to the formation of the CaO oxide. Starting from the temperature of about 880 °C, the mass decreased smoothly likely due to the removal of interstitial fluorine ions from NPs. A slight endothermal peak associated with the phase transformation in an unknown compound was observed in the DSC curve at the temperature of 680 °C. This peak likely corresponds to the phase transition between polymorphous forms of manganese oxide.

Thus, the thermal analysis has shown that the as-prepared sample contains the rather large amount of carbonaceous impurities and water molecules, which could be removed at the longer annealing (in our case, the short 10-min annealing was used) without a considerable increase in the nanocrystal growth.

3.6. Upconversion spectra

The upconversion spectra of CaF_2:Mn/Yb/Er/Si recorded under the laser (λ = 980 nm) excitation at the room temperature are shown in Fig. 4a. The spectra of Er^{3+} ions of each sample include seven emission peaks at ~432, ~490, ~543, ~595 ~611, ~674, and ~ 837 nm. The spectrum of the S900 sample includes an additional peak at 453.7 nm. Fig. 4a shows the assignment of the spectral lines. Er^{3+} luminescence is sensitized in the presence of Yb^{3+} due to the intense absorption of laser radiation of 980 nm $^2F_{7/2} \rightarrow {}^2F_{5/2}$, followed by energy transfer to Er^{3+} in the $^4I_{11/2}$ state. The $^4I_{11/2} \rightarrow {}^4F_{7/2}$ transition also occurs upon excitation by the second photon from the $^2F_{5/2}$ state of the Yb^{3+} ion. The $^4F_{9/2}$ state of the Er^{3+} ion is excited directly by two laser photons with the participation of the matrix phonons.

In the transfer of excitation energy between Er^{3+} ions, the cross-relaxation process $^4I_{11/2} + {}^4I_{11/2} \rightarrow {}^4I1_{5/2} + {}^4F_{7/2}$ is dominant, which equally affects the population of levels $^2H_{11/2}$, $^4S_{3/2}$.

For the S900 sample, the $^4F_{5/2} - {}^4I_{15/2}$ transition, practically absent for all the other samples, is observed. An increase in the probability of population of the $^4F_{5/2}$ level is likely caused by the change in the structure of optical centers at the annealing at 900 °C.

The PL intensity of the samples changes nonmonotonically with an increase of the annealing temperature (growth of the nanoparticle size) (Fig. 4b). The annealing at 200 °C has led to the removal of water adsorbed inside mesopores and on the surface of NPs. It is well-known [68] that water can significantly quench luminescence. The short (10 min) annealing of NPs at the temperature of 200 °C should not lead to considerable growth of nanoparticle size, which is in agreement with the data of SEM microscopy. Therefore, an increase in the emission intensity of the S200 sample was not caused by an increase in the size of nanocrystals. However, the significant increase of the SSA of NP was observed in the S200 sample (Table. 4). This increase of the SSA can be explained exclusively by desorption of water and other volatile compounds from the sample surface and mesopores. That is why the luminescence intensity of the S200 sample increased markedly, especially, in the red and NIR peaks.

The annealing at 400 °C has led to a decrease in the emission intensity of the red and NIR peaks. At the same time, the intensity of all other peaks exceeded the intensity of the corresponding peaks in the dominant S200 sample. The further increase of the annealing temperature has led to a sharp decrease of the integral PL intensity in the S600 and S900 samples. The marked splitting of all peaks in the spectrum of the S600 sample is indicative of the change in the crystalline field at the optical centers. Distortions of the crystal lattice were caused, in their turn, by the growth of the additional CaO phase. The change in the valence of Mn^{2+} ions residing directly on the surface of NPs (which is clearly seen from the permanent change in the color of the as-prepared S0 sample from the white-beige to black in the S900 sample) decreases the PL intensity of CaF_2:Mn/Yb/Er/Si NPs. The similar change in the color of the as-prepared non-annealed sample from white at the room temperature (RT) to deep black after annealing at 800 °C was observed in [60]. A significant decrease in the intensity of all seven PL peaks of Er^{3+} ions and appearance of the new blue peak (453.7 nm) in the S900 sample is connected with the change in the phase composition of nanopowder at the high-temperature (900 °C) annealing, namely, formation of additional CaO and MnO_2 phases, which supports the correctness of the proposed way of phase transformation in the samples during the annealing.

A change in the intensity ratio of the red (673 nm) to green (543 nm) bands (R_{673}/G_{543}) and the NIR band (837 nm) to red (673 nm) bands NIR_{837}/R_{673} with an increase of the annealing temperature is depicted in Fig. 4b, c. One can see that the integral PL intensity of the S200 sample (total of all 7 peaks) is nearly twice as high as the intensity of the S0 sample. Therefore, it must be conceded that from the viewpoint of the possible use of the NIR-to-NIR upconversion of CaF_2:Mn/Yb/Er/Si NPs in NIR-to-NIR theranostics [69], the S200 sample is most suitable for bio-imaging and drug delivery (as a nano-container).

It is well-known [5,70,71] that the significant increase of the emission intensity in the red band (650 nm) can be achieved through an increase in the concentration of Mn^{2+} ions in the fluoride lattice. It was shown in [5] that the addition of different Mn^{2+} dopant contents in $NaLnF_4$:Yb/Er (Ln = Ln: Lu, Gd, Yb) resulted in the high UCPL intensity, which was 59.1 times higher than the UCPL intensity of the sample containing no Mn.

UCPL in NIR-to-Red or NIR - NIR [69,72–74] spectral ranges has the prime importance at the exciting radiation with the wavelength of about 800 – 980 nm. This case is of particular significance for biomedical purposes. The excitation in the NIR spectral range in combination with the emission of UCNPs themselves in the NIR or Red ranges is very promising due to the high transparency of biological liquids, low tissue damage, and nearly complete absence of autofluorescence [75]. In addition, UCPL of Ln^{3+}-doped inorganic NPs has many desirable properties, such as the high quantum efficiency of luminescence, long lifetime of excited states, and high photostability [76].

Thus, two intense peaks in the NIR (837 nm) and RED (657 nm) ranges have been found in the UCPL spectrum of CaF_2:Mn/Yb/Er/Si NPs. The emission of these peaks can be used in photodynamic therapy (PDT) for excitation of a photosensitizer (PS) located in the disease

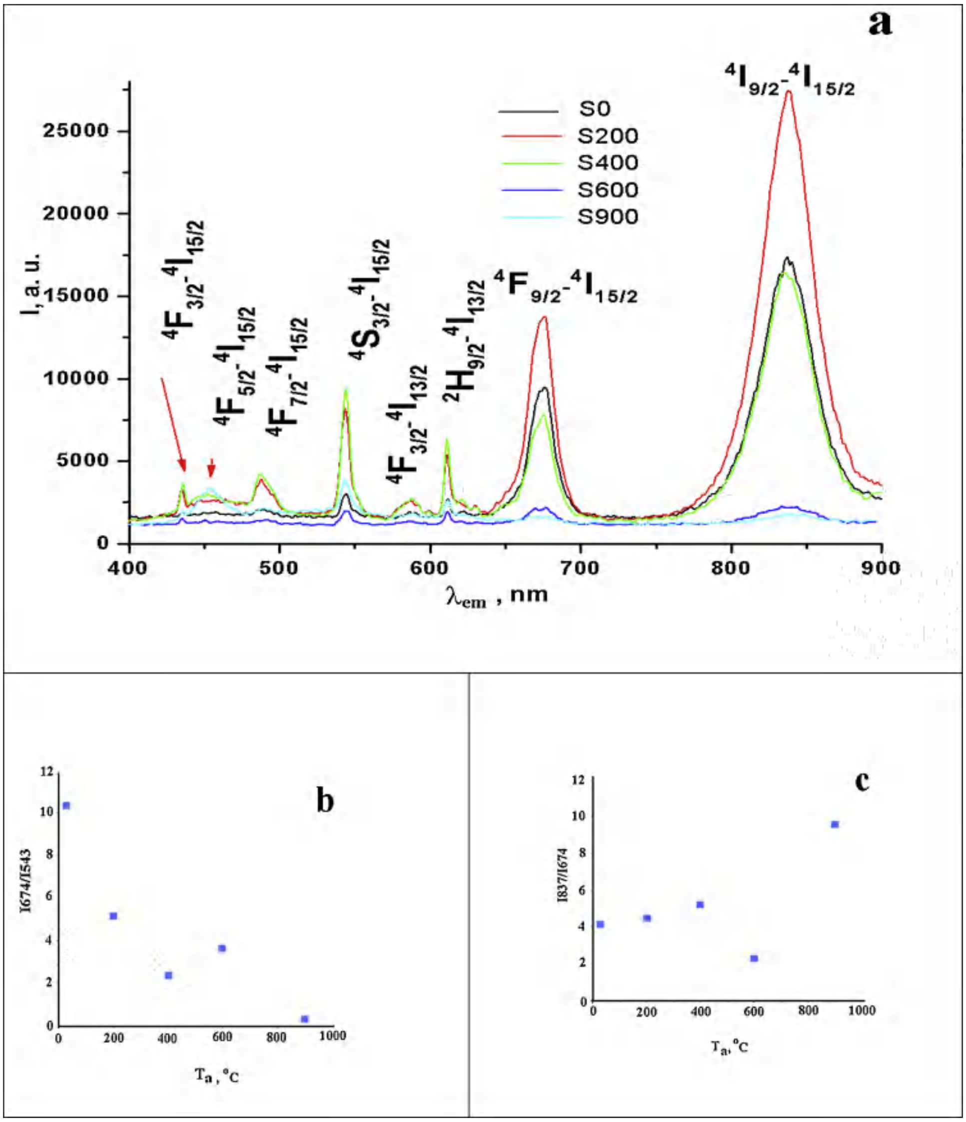

Fig. 4. a) Upconversion emission spectra (λ_{exc} = 980 nm) of CaF_2:Mn/Yb/Er/Si NPs; **b)** the calculated Red/Green ratio; c) the calculated NIR/Red ratio.

area. In this case, it is possible to use simultaneously two and more photosensitizers [77] having the absorption spectra in the NIR and RED ranges. The photodynamic therapy (PDT) uses special preparations referred to as photosensitizing agents, which reacts to the certain type of radiation, to kill cancer cells [78].

The new generation of photosensitizers is now actively developed. They have stronger absorption in the NIR spectral range corresponding to the optimal transmission window of bio-tissues (700 − 1000 nm) [79].

3.7. Magnetic properties

All the CaF_2: Mn/Yb/Er samples before and after the annealing demonstrated paramagnetic properties at the room temperature (Fig. 5). At the room temperature, the magnetization curves are linear functions of the field. This allows us to determine the susceptibility and to compare it with the value calculated from the concentration of Mn ions on the assumption that the valent state is 2+ (high-spin state, S = 5/2). In this case, the calculation yields the value of 2.3 10^{-5} cm^3/g, which markedly exceeds the experimental values (Table 5).

The discrepancy between the calculated and experimental values of susceptibility may be connected with the low-spin state of some Mn atoms. However, it should be noted that according to the literature data

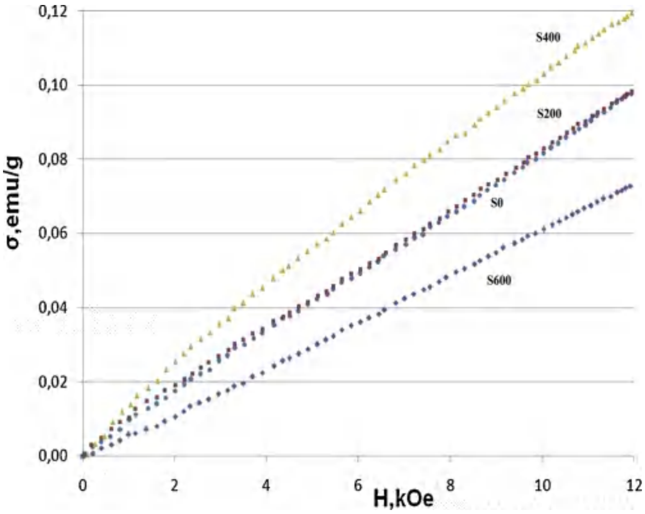

Fig. 5. Magnetization curves of the S0, S200, S400, and S600 samples as measured at 300 K.

Table 5
Magnetic susceptibility of CaF_2:Mn/Yb/Er/Sibefore and after annealing.

Sample	Susceptibility, 10^{-6} cm^3/g
S0	8.1(4)
S200	8.1(4)
S 400	9.1(4)
S 600	6.3(3)
SO (calculation)	23

[80] the low-spin state is observed quite rarely for Mn^{2+} because it requires the presence of a strong crystal field. Another possible cause for the decrease of susceptibility can be anti-ferromagnetic interaction between closely spaced manganese ions [81]. A change in the structure at annealing can affect both the spin state of manganese ions and their mutual arrangement, and the both these factors can be causes for the change in susceptibility as a result of annealing at 400 and 600 °C.

4. Conclusions

Thus, multimodal (UCNP/MRI/CT) CaF_2: Mn/Yb/Er /Si NPs have been synthesized by the PEBE method in a vacuum. The NPs have demonstrated the dominant RED-NIR upconversion luminescence under the irradiation by a 980-nm laser. Mesoporous CaF_2:Mn/Yb/Er/Si NPs were characterized by the large volume of inter-particle pores (up to 2 cm^3/g). Thus, they can be used as nano-containers, for example, for drug storage and delivery. The paramagnetic properties of CaF_2:Mn/Yb/Er/Si NPs suggests the possibility of their use in MRI. The presence of Yb in the composition of NPs assumes their possible use in CT as a contrast agent [33]. The minimal content of REE ions in the composition of NPs allows us to hope of their low toxicity for living cells The study of the effect of annealing of NPs in the air has confirmed the high thermal stability of NPs in the temperature range from RT to 400 °C. Potentially, the developed NPs can be used as a trimodal agent in UCPL/MR/CT imaging.

The effect of thermal processing of NPs on their structural, textural, luminescent, and magnetic properties has been examined. It has been found that NIR-to-NIR and NIR-VIS upconversion photoluminescence (UCPL) of NPs before and after annealing was observed under the excitation by a 980-nm laser. The intensity of the UCPL peaks in the NIR and VIS spectral ranges changed in different directions with an increase of the annealing temperature (with an increase of the particle size). The maximal UC intensity of the peak in the NIR range was observed after annealing of the sample at the temperature 200 °C, while the maximal intensity in the visible range was observed after annealing at the temperature of 400 °C. The sharp increase of the integral UCPL intensity in the range 300 − 900 nm was observed after annealing at the temperature of 600 and 900 °C. The suppression of UC luminescence of both types with an increase of the annealing temperature was caused by the change in the phase composition of NPs (formation of CaO oxide, the appearance of the Mn_3O_4 spinel phase on the surface of NPs) and in the valence of Mn^{2+} ions to Mn^{3+} and Mn^{4+}. The upconversion luminescence lines of the NPs include radiation at the wavelength of 837 nm, which is very promising for these NPs to be used for object imaging in bio-tissues. Owing to the optical properties of these nanophosphors, they can be excited directly through bio-tissue and, in addition, the zone of their location can be seen [82].

Declaration of Competing Interest

Authors have no conflict of interest From the team of authors Dr. Ilves

Acknowledgments

The work was supported by the Ministry of Science and Education of the Russian Federation (Federal Task Project No. 0389-2015-0026) and by the Russian Foundation for Basic Research (Grant No. 18-08-00514). This research was supported by the Institutional Research Funding (IUT2-24 and IUT20-54) and by the Namur+Project of the Ministry of Education and Research of the Republic of Estonia. The magnetic measurements were performed within the framework of the government assignment (Magnet Theme No. AAAA-A18-118020290129-5).

Appendix A. Supplementary data

Supplementary material related to this article can be found, in the online version, at doi:https://doi.org/10.1016/j.jfluchem.2020.109457.

References

[1] Y. Liu, D. Tu, H. Zhu, E. Ma, X. Chen, Lanthanide-doped luminescent nano-bioprobes: from fundamentals to biodetection, Nanoscale 5 (2013) 1369–1384, https://doi.org/10.1039/C2NR33239F.

[2] N. Erathodiyil, J.Y. Ying, Functionalization of inorganic nanoparticles for bioimaging applications, Acc. Chem. Res. 44 (2011) 925–935, https://doi.org/10.1021/ar2000327.

[3] J. Kim, Y. Piao, T. Hyeon, Multifunctional nanostructured materials for multimodal imaging, and simultaneous imaging and therapy, Chem. Soc. Rev. 38 (2009) 372–390, https://doi.org/10.1039/b709883a.

[4] G. Wang, Q. Peng, Y. Li, Lanthanide-doped nanocrystals: synthesis, optical-magnetic properties and applications, Acc. Chem. Res. 44 (2011) 322–332, https://doi.org/10.1021/ar100129p.

[5] S. Zeng, Z. Yi, W. Lu, C. Qian, H. Wang, L. Rao, T. Zeng, H. Liu, H. Liu, B. Fei, J. Hao, Simultaneous realization of phase/size manipulation, upconversion luminescence enhancement, and blood vessel imaging in multifunctional nanoprobes through transition metal Mn^{2+} doping, Adv. Funct. Mater. 24 (2014) 4051–4059, https://doi.org/10.1002/adfm.201304270.

[6] Y. Liu, X. Meng, W. Bu, Upconversion-based photodynamic cancer therapy, Coord. Chem. Rev. 379 (2019) 82–98, https://doi.org/10.1016/j.ccr.2017.09.006.

[7] J. Wang, F. Wang, C. Wang, Z. Liu, X. Liu, Single-band upconversion emission in lanthanide-doped $KMnF_3$ nanocrystals, Angew. Chem. Int. Ed. 50 (2011) 10369–10372, https://doi.org/10.1002/anie.201104192.

[8] P. Woźny, M. Runowski, S. Lis, Emission color tuning and phase transition determination based on high pressure up-conversion luminescence in YVO_4: Yb^{3+}, Er^{3+} nanoparticles, J. Lumin. 209 (2019) 321–327, https://doi.org/10.1016/j.jlumin.2019.02.008.

[9] G.S. Yi, G.M. Chow, Synthesis of hexagonal-phase $NaYF_4$:Yb,Er and $NaYF_4$:Yb,Tm nanocrystals with efficient up-conversion fluorescence, Adv. Funct. Mater. 16 (2006) 2324–2329, https://doi.org/10.1002/adfm.200600053.

[10] X. Wu, G. Chen, J. Shen, Z. Li, Y. Zhang, G. Han, Upconversion nanoparticles: a versatile solution to multiscale biological imaging, Bioconjugate Chem. 26 (2015) 166–175, https://doi.org/10.1021/bc5003967.

[11] H. Xing, W. Bu, S. Zhang, X. Zheng, M. Li, F. Chen, Q. He, L. Zhou, W. Peng, Y. Hua, J. Shi, Multifunctional nanoprobes for upconversion fluorescence, MR and CT trimodal imaging, Biomaterials 33 (2012) 1079–1089, https://doi.org/10.1016/j.biomaterials.2011.10.039.

[12] J. Zhou, Y. Sun, X. Du, L. Xiong, H. Hu, F. Li, Dual-modality in vivo imaging using rare-earth nanocrystals with near-infrared to near-infrared (NIR-to-NIR)upconversion luminescence and magnetic resonance properties, Biomaterials 31 (2010) 3287–3295, https://doi.org/10.1016/j.biomaterials.2010.01.040.

[13] Y. Sun, X. Zhu, J. Peng, F. Li, Core-shell lanthanide upconversion nanophosphors as four-modal probes for tumor angiogenesis imaging, ACS Nano 7 (2013) 11290–11300, https://doi.org/10.1021/nn405082y.

[14] J. Zhou, X.J. Zhu, M. Chen, Y. Sun, F.Y. Li, Water-stable NaLuF4-based upconversion nanophosphors with long-term validity for multimodal lymphatic imaging, Biomaterials 33 (2012) 6201–6210, https://doi.org/10.1016/j.biomaterials.2012.05.036.

[15] Q. Liu, Y. Sun, C. Li, J. Zhou, C. Li, T. Yang, X. Zhang, T. Yi, D. Wu, F. Li, ^{18}F-Labeled magnetic-upconversion nanophosphors via rare-Earth cation-assisted ligand assembly, ACS Nano 5 (2011) 3146–3157, https://doi.org/10.1021/nn200298.

[16] Z. Li, Y. Zhang, L. Huang, Y. Yang, Y. Zhao, G. El-Banna, G. Han, Nanoscale “fluorescent stone”: luminescent calcium fluoride nanoparticles as theranostic platforms, Theranostics 6 (2016) 2380–2393, https://doi.org/10.7150/thno.15914.

[17] J.L. Vivero-Escoto, R.C. Huxford-Phillips, W. Lin, Silica-based nanoprobes for biomedical imaging and theranostic applications, Chem. Soc. Rev. 41 (2012) 2673–2685, https://doi.org/10.1039/c2cs15229k.

[18] X. Huang, P.K. Jain, I.H. El-Sayed, M.A. El-Sayed, Gold nanoparticles: interesting optical properties and recent applications in cancer diagnostics and therapy, Nanomedicine 2 (2007) 681–693, https://doi.org/10.2217/17435889.2.5.681.

[19] W. Zheng, S. Zhou, Z. Chen, P. Hu, Y. Liu, D. Tu, H. Zhu, R. Li, M. Huang, X. Chen,

Sub-10 nm lanthanide-doped CaF_2 nanoprobes for time-resolved luminescent biodetection, Angew. Chem. Int. Ed. 52 (2013) 6671–6676, https://doi.org/10.1002/anie.201302481.

[20] D.T. Tu, L.Q. Liu, Q. Ju, Y.S. Liu, H.M. Zhu, R.F. Li, X.Y. Chen, Time-resolved FRET biosensor based on amine functionalized lanthanide doped $NaYF_4$ nanocrystals, Angew. Chem. Int. Ed. 50 (2011) 6306–6310, https://doi.org/10.1002/ange.201100303.

[21] V.E. Kafadar, A.N. Yazici, R.G. Yildirim, Fabrication, properties and thermo-luminescent dosimetric application of CaF_2:Mn transparent ceramic, Nucl. Instrum. Methods Phys. Res. Sect. B 267 (2009) 3337–3346, https://doi.org/10.1016/j.nimb.2012.06.002.

[22] M. Zahedifar, E. Sadeghi, Z. Mohebbi, Synthesis and thermoluminescence characteristics of Mn doped CaF_2 nanoparticles, Nucl. Instrum. Methods Phys. Res. Sect. B 274 (2012) 162–166, https://doi.org/10.1016/j.nimb.2011.12.015.

[23] G. Tian, Z. Gu, L. Zhou, W. Yin, X. Liu, L. Yan, S. Jin, W. Ren, G. Xing, S. Li, Y. Zhao, Mn^{2+} dopant-controlled synthesis of $NaYF_4$:Yb/Er upconversion nanoparticles for in vivo imaging and drug delivery, Adv. Mater. (Weinheim, Ger.) 24 (2012) 1226–1231, https://doi.org/10.1002/adma.201104741 Epub 2012 Jan 27.

[24] X. Deng, Y. Dai, J. Liu, Y. Zhou, Multifunctional hollow $CaF_2:Yb^{3+}/Er^{3+}/\ Mn^{2+}$-poly(2-Aminoethyl methacrylate) microspheres for Pt(IV) pro-drug delivery and tri-modal imaging, Biomaterials 50 (2015) 154–163, https://doi.org/10.1016/j.biomaterials.2015.01.040.

[25] H. Wang, W. Lu, Z. Yi, L. Rao, S. Zeng, Z. Li, Enhanced upconversion luminescence and single-band red emission of $NaErF_4$ nanocrystals via Mn^{2+} doping, J. Alloys Compd. 618 (2015) 776–780, https://doi.org/10.1016/j.jallcom.2014.08.174.

[26] M. Haase, H. Schäfer, Upconverting nanoparticles, Angew. Chem. Int. Ed. 50 (2011) 5808–5829, https://doi.org/10.1002/anie.201005159.

[27] K. Liu, X. Yan, Y.J. Xu, L. Dong, L.N. Hao, Y.H. Song, F. Li, Y. Su, Y.D. Wu, H.S. Qian, W. Tao, X.Z. Yang, W. Zhou, Y. Lu, Sequential growth of CaF_2:Yb,Er@CaF_2:Gd nanoparticles for efficient magnetic resonance angiography and tumor diagnosis, Biomater. Sci. 5 (2017) 2403–2415, https://doi.org/10.1039/c7bm00797c.

[28] Y. Li, Y. Gu, W. Yuan, T. Cao, K. Li, S. Yang, Z. Zhou, F. Li, Simultaneous enhancement of photoluminescence, MRI relaxivity, and CT contrast by tuning the interfacial layer of lanthanide heteroepitaxial nanoparticles, ACS Appl. Mater. Interfaces 8 (2016) 19208–19216, https://doi.org/10.1021/acs.nanolett.7b01753.

[29] I.X. Cantarelli, M. Pedroni, F. Piccinelli, P. Marzola, F. Boschi, G. Conti, A. Sbarbati, P. Bernardi, E. Mosconi, L. Perbellini, L. Marongiu, M. Donini, S. Dusi, L. Sorace, C. Innocenti, E. Fantechi, C. Sangregoriog, A. Speghini, Multifunctional nanoprobes based on upconverting lanthanide doped CaF2: towards biocompatible materials for biomedical imaging, Biomater. Sci. 2 (2014) 1158–1171, https://doi.org/10.1039/C4BM00119B.

[30] A. Li, M. Lu, J. Yang, L. Chen, X. Cui, X. Sun, Upconversion-luminescent/magnetic dual-functional sub-20 nm core-shell SrF_2:Yb,Tm@CaF_2:Gd heteronanoparticles, DaltonTrans. 45 (2016) 5800–5807, https://doi.org/10.1039/C6DT00237D.

[31] X. Qiao, J. Zhou, J. Xiao, Y. Wang, L. Sun, C. Yan, Triple-functional core-shell structured upconversion luminescent nanoparticles covalently grafted with photosensitizer for luminescent, magnetic resonance imaging and photodynamic therapy in vitro, Nanoscale 4 (2012) 4611–4623, https://doi.org/10.1039/c2nr30938f.

[32] S.Yu. Sokovnin, V.G. Il'ves, Production of nanopowders using pulsed electron beam, Ferroelectrics 436 (2012) 101–107, https://doi.org/10.1080/10584587.2012.730951.

[33] N. Lee, S.H. Choi, T. Hyeon, Nano-sized CT contrast agents, Adv. Mater. (Weinheim, Ger.) 25 (2013) 2641–2660, https://doi.org/10.1002/adma.201300081.

[34] N. Bogdan, F. Vetrone, G.A. Ozin, J.A. Capobianco, Synthesis of ligand-free colloidally stable water dispersible brightly luminescent lanthanide-doped upconverting nanoparticles, Nano Lett. 11 (2011) 835–840, https://doi.org/10.1021/nl1041929.

[35] T.Y. Cao, Y. Yang, Y. Gao, J. Zhou, Z.Q. Li, F.Y. Li, High-quality water-soluble and surface-functionalized upconversion nanocrystals as luminescent probes for bioimaging, Biomaterials 32 (2011) 2959–2968, https://doi.org/10.1016/j.biomaterials.2010.12.050.

[36] Y. Min, J. Liu, P. Padmanabhan, E. Yeow, B. Xing, Recent of biological molecular imaging based on lanthanide-doped upconversion-luminescent nanomaterials, Nanomaterials 4 (2014) 129–154, https://doi.org/10.3390/nano4010129.

[37] M.-A. Fortin, Magnetic nanoparticles used as contrast agents in MRI: relaxometric characterization, in: S.S.R. Kumar (Ed.), Magnetic Characterization Techniques for Nanomaterials, Springer-Verlag, Berlin Heidelberg, 2017, pp. 511–555, , https://doi.org/10.1007/978-3-662-52780-1_15.

[38] N.N. Dong, M. Pedroni, F. Piccinelli, G. Conti, A. Sbarbati, J.E. Ramírez- Hernández, L.M. Maestro, M.C. Iglesias-de la Cruz, F. Sanz-Rodriguez, A. Juarranz, NIR-to-NIR two-photon excited CaF_2: Tm^{3+}, Yb^{3+} nanoparticles: multifunctional nanoprobes for highly penetrating fluorescence bio-imaging, ACS Nano 5 (2011) 8665–8671, https://doi.org/10.1021/nn202490m.

[39] I. Etchart, A. Huignard, M. Bérard, M.N. Nordin, I. Hernández, R.J. Curry, W.P. Gillind, A.K. Cheetham, Oxide phosphors for efficient light upconversion: Yb^{3+} and Er^{3+} co-doped Ln_2BaZnO_5 (Ln = Y, Gd), J. Mater. Chem. 20 (2010) 3989–3994, https://doi.org/10.1039/C000127A.

[40] K. Chakrabarti, J. Sharma, V.K. Mathur, J.H. Barkyoumb, Optical properties of radiation defect centers involving single and paired Mn^{2+} centers in CaF_2:Mn, Phys. Rev. B Condens. Matter 51 (1995) 16541–16548, https://doi.org/10.1103/PhysRevB.51.16541.

[41] J.M.C. Marco de Lucasy, M. Morenoy, F. Rodriguezy, P.G. Baranov, Luminescence from BaF_2Mn_2C samples: substitutional Mn_2C ions are 'silent', J. Phys. Condens. Matter 8 (1996) 2457–2465.

[42] D.D. Ikrami, P.P. Fedorov, A.A. Luginina, L.A. Olkhovaya, MgF_2-MnF_2, CaF_2-MnF_2, SrF_2-MnF_2 systems, J. Biol. Inorg. Chem. 30 (1985) 1261–1265 (In Russian) https://www.researchgate.net/publication/266022130_MgF2-MnF2_CaF2-MnF2_SrF2-MnF2_SYSTEMS.

[43] P.P. Fedorov, V.V. Osiko, S.V. Kuznetsov, E.A. Garibin, Fluoride laser nanoceramics, IV nanotechnology international forum (rusnanotech 2011) IOP publishing, J. Phys. Conf. Ser. 345 (2012) 012017, , https://doi.org/10.1088/1742-6596/345/1/012017.

[44] A.A. Luginina, P.P. Fedorov, Synthesis of ultrafine fluorite powders phases $Ca_{1-x}R_xF^{2+}{}_x$ (R = Nd, Er, Yb) by chemical precipitation from aqueous solutions, Khim. Tekhnol. 12 (2011) 264–270 (in Russian).

[45] R.D. Shannon, Revised effective ionic radii and systematic studies of interatomic distances in halides and chalcogenides, Acta Crystallogr. Sect. A 32 (1976) 751–767, https://doi.org/10.1107/S0567739476001551.

[46] B.P. Sobolev, A.M. Golubev, P. Herrero, Fluorite $M_{1-x}R_xF_{2+x}$ phases (M = Ca, Sr, Ba; R = rare earth elements) as nanostructured materials, Crystallogr. Rep. 48 (2003) 141–161, https://doi.org/10.1134/1.1541755.

[47] N.C. Dyck, F.C.J.M. van Veggel, G.P. Demopoulos, Size dependent maximization of upconversion efficiency of citrate-stabilized β-phase $NaYF_4:Yb^{3+}Er^{3+}$ crystals via annealing, ACS Appl. Mater. Interfaces 5 (2013) 11661–11667, https://doi.org/10.1021/am403100t.

[48] R.A. Jesus, A.S. Rabelo, R.T. Figueiredo, L.C. Cides da Silva, I.C. Codentino, M.C.A. Fantini, G.L.B. Araújo, A.A.S. Araújo, M.E. Mesquita, Synthesis and application of the MCM-41 and SBA-15 as matrices for in vitro efavirenz release study, J. Drug Deliv. Sci. Technol. 31 (2016) 153–159, https://doi.org/10.1016/j.jddst.2015.11.008.

[49] V.G. Il'ves, M.G. Zuev, S.Yu. Sokovnin, A.M. Murzakaev, Properties of an amorphous silicon dioxide nanopowder prepared by pulsed electron beam evaporation, Phys. Solid State 57 (2015) 2512–2518, https://doi.org/10.1134/S1063783415120161.

[50] S.Y. Sokovnin, V.G. Il'ves, M.G. Zuev, M.A. Uimin, Magnetic and luminescent properties of barium fluoride nanopowder obtained by electron-beam evaporation in low-pressure gas, Tech. Phys. Lett. 44 (2018) 765–768, https://doi.org/10.1134/S1063785018090122.

[51] V.G. Il'ves, S.Y. Sokovnin, S.A. Uporov, M.G. Zuev, Properties of the amorphous-nanocrystalline Gd_2O_3 powder prepared by pulsed electron beam evaporation, Phys. Solid State 55 (2013) 1262–1271, https://doi.org/10.1134/S1063783413060127.

[52] S.Y. Sokovnin, V.G. Il'ves, M.G. Zuev, Production of complex metal oxide nanopowders using pulsed electron beam in Low-pressure gas for biomaterials application, in: A.M. Grumezescu (Ed.), Engineering of Nanobiomaterials Applications of Nanobiomaterials, Vol. 2 Elsevier, Amsterdam, 2016, pp. 29–75, , https://doi.org/10.1016/B978-0-323-41532-3.00002-6.

[53] AEROSIL® – Fumed Silica, Technical Overview, (2020) https://www.aerosil.com/sites/lists/RE/DocumentsSI/Technical-Overview-AEROSIL-Fumed-Silica-EN.pdf.

[54] S.Y. Sokovnin, V.G. Il'ves, S.V. Zayats, M.G. Zuev, Properties of compacts of barium fluoride nanopowder produced by pulsed electron beam evaporation, Ceram. Int. 45 (2019) 16591–16599, https://doi.org/10.1016/j.ceramint.2019.05.198.

[55] W.A. Bala, V.S. Benitha, K. Jeyasubramanian, G.S. Hikku, P. Sankar, S.V. Kumar, Investigation of anti-bacterial activity and cytotoxicity of calcium fluoride nanoparticles, J. Fluorine Chem. 193 (2017) 38–44, https://doi.org/10.1016/j.jfluchem.2016.11.014.

[56] C. Pandurangappa, B. Lakshminarasappa, B. Nagabhushana, Synthesis and characterization of CaF_2 nanocrystals, J. Alloys Compd. 489 (2010) 592–595, https://doi.org/10.1016/j.jallcom.2009.09.118.

[57] S. Rungrodnimitchai, Novel synthesis of CaF_2 nanocrystals and the effect of pyridine addition on their crystal size, J. Appl. Phys. 50 (2011) 01J17, , https://doi.org/10.1143/JJAP.50.01BJ17.

[58] M. Pedroni, F. Piccinelli, T. Passuello, M. Giarol, G. Mariotto, S. Polizzi, M. Bettinelli, A. Speghini, Lanthanide doped upconverting colloidal CaF_2 nanoparticles prepared by a single-step hydrothermal method: toward efficient materials with near infrared-to-near infrared upconversion emission, Nanoscale 3 (2011) 1456–1460, https://doi.org/10.1039/C0NR00860E.

[59] A. Bensalah, M. Mortier, G. Patriarche, P. Gredin, D. Vivine, Synthesis and optical characterizations of undoped and rare-earth-doped CaF_2 nanoparticles, J. Solid State Chem. 179 (2006) 2636–2644, https://doi.org/10.1016/j.jssc.2006.05.011.

[60] P.D. Sahare, M. Singh, P. Kumar, Effect of annealing and impurity concentration on the TL characteristics of nanocrystalline Mn-doped CaF_2, Radiat. Meas. 80 (2015) 29–37, https://doi.org/10.1016/j.radmeas.2015.07.003.

[61] N.S.C. Zulkifli, I.A. Rahmann, D. Mohamad, A. Husein, A green sol-gel route for the synthesis of structurally controlled silica particles from rice husk for dental composite filler, Ceram. Int. l39 (2013) 4559–4567, https://doi.org/10.1016/j.ceramint.2012.11.052.

[62] P. Yang, S. Gai, J. Lin, Functionalized mesoporous silica materials for controlled drug delivery, Chem. Soc. Rev. 41 (2012) 3679–3698, https://doi.org/10.1039/c2cs15308d.

[63] X. Kang, Z. Cheng, C. Li, D. Yang, M. Shang, P. Ma, G. Li, N. Liu, J. Lin, Core-shell structured up-conversion luminescent and mesoporous $NaYF_4:Yb^{3+}/Er^{3+}$@nSiO_2@mSiO_2 nanospheres as carriers for drug delivery, J. Phys. Chem. C 115 (2011) 15801–15811, https://doi.org/10.1021/jp203039t.

[64] Y. Li, Y. Zhou, X. Lia, J. Sun, Z. Ren, W. Wen, X. Yang, G. Han, A facile approach to upconversion crystalline $CaF_2:Yb^{3+}Tm^{3+}$@mSiO_2 nanospheres for tumor therapy, RSC Adv. 6 (2016) 38365–38370, https://doi.org/10.1039/C6RA04167A.

[65] F. Zhang, Y. Wan, Y.F. Shi, B. Tu, D.Y. Zhao, Ordered mesostructured rare-earth fluoride nanowire arrays with upconversion fluorescence, Chem. Mater. 20 (2008) 3778–3784, https://doi.org/10.1021/cm800489e.

[66] N. Hao, F. Tang, L. Li, MCM-41 mesoporous silica sheet with ordered perpendicular

nanochannels for protein delivery and the assembly of Ag nanoparticles in catalytic applications, Microporous Mesoporous Mater. 218 (2015) 223–227, https://doi.org/10.1016/j.micromeso.2015.06.023.

[67] I. Izquierdo-Barba, E. Sousa, J. Carlos Doadrio, A. Luis Doadrio, J. Pérez Pariente, A. Martínez, F. Babonneau, M. Vallet-Regí, Influence of mesoporous structure type on the controlled delivery of drugs: release of ibuprofen from MCM-48, SBA-15 and functionalized SBA-15, J. Solgel Sci. Technol. 50 (2009) 421–429, https://doi.org/10.1007/s10971-009-1932-3.

[68] I.L.V. Estrada, R. Narro-Garcia, T. Lopez-Luke, V.H. Romero, J.A. Christen, E. de La Rosa, Synthesis and luminescence properties of TiO_2:Yb–Er mesoporous nanoparticles, Bull. Mater. Sci. 41 (8) (2018) 110, https://doi.org/10.1007/s12034-018-1615-1.

[69] X. Chen, Y. Tang, A. Liu, Y. Zhu, D. Gao, Y. Yang, J. Sun, H. Fan, X. Zhang, NIR-to-red upconversion nanoparticles with minimized heating effect for synchronous multidrug resistance tumor imaging and therapy, ACS Appl. Mater. Interfaces 10 (2018) 14378–14388, https://doi.org/10.1021/acsami.8b00409.

[70] Y.M. Li, S. Qi, P.L. Li, Z.J. Wang, Research progress of Mn doped phosphors, RSC Adv. 7 (2017) 38318–38334, https://doi.org/10.1039/C7RA06026B.

[71] J. Zhang, S. Wang, N. Gao, D. Feng, L. Wang, H. Chen, Luminescence energy transfer detection of PSA in red region based on Mn^{2+}-enhanced $NaYF_4$:Yb, Er upconversion nanorods, Biosens. Bioelectron. 72 (2015) 282–287, https://doi.org/10.1016/j.bios.2015.05.024.

[72] S. Wu, J.P. Blinco, C. Barner-Kowolli, Near-infrared photoinduced reactions assisted by upconverting nanoparticles, Chem. Eur. J. 23 (2017) 8325–8332, https://doi.org/10.1002/chem.201700658.

[73] C. Wang, H. Tao, L. Cheng, Z. Liu, Near-infrared light induced in vivo photodynamic therapy of cancer based on upconversion nanoparticles, Biomaterials 32 (2011) 6145e6154, , https://doi.org/10.1002/adfm.201304270.

[74] Y. Lv, Y. Jin, T. Sun, J. Su, C. Wang, G. Ju, L. Chen, Y. Hu, Visible to NIR down-shifting and NIR to visible upconversion luminescence in $Ca_{14}Zn_6Ga_{10}O_{35}$:Mn^{4+}, Ln^{3+} (Ln = Nd, Yb, Er), Dye. Pigments 161 (2019) 137–146, https://doi.org/10.1016/j.dyepig.2018.09.052.

[75] A.N. Generalova, B.N. Chichkov, E.V. Khaydukov, Multicomponent nanocrystals with anti-Stokes luminescence as contrast agents for modern imaging techniques, Adv. Colloid Interface Sci. 245 (2017) 1–19, https://doi.org/10.1016/j.cis.2017.05.006.

[76] O. Ehlert, R. Thomann, M. Darbandi, T. Nann, A four-color colloidal multiplexing nanoparticle system, ACS Nano 2 (2008) 120–124, https://doi.org/10.1021/nn7002458.

[77] E.A. Sagaidachnaya, I.Y. Yanina, V.I. Kochubey, Prospects for application of up-conversion particles NaYF4:Er,Yb for phototherapy, izv. Saratov University, New Ser. Ser: Phys. 4 (2018) 253–274 (In Russian), https://fizika.sgu.ru/en/journal/2018/4.

[78] Z. Huang, H. Xu, A.D. Meyers, A.I. Musani, L. Wang, R. Tagg, A.B. Barqawi, Y.K. Chen, Photodynamic therapy for treatment of solid tumors—Potential and technical challenges, Technol. Cancer Res. Treat. 7 (2008) 309–320, https://doi.org/10.1177/153303460800700405.

[79] L. Luan, L. Ding, W. Zhang, J. Shi, X. Yu, W. Liu, A naphthalocyanine based near-infrared photosensitizer: synthesis and in vitro photodynamic activities, Bioorg. Med. Chem. Lett. 23 (2013) 3775–3779, https://doi.org/10.1016/j.bmcl.2013.04.093.

[80] I. Syiemlieh, A. Kumar, S.D. Kurbah, A.K. De, R.A. Lal, Low-spin manganese(II) and high-spin manganese(III) complexes derived from disalicylaldehyde oxaloyldihydrazone: synthesis, spectral characterization and electrochemical studies, J. Mol. Struct. 1151 (2018) 343–352, https://doi.org/10.1016/j.molstruc.2017.09.052.

[81] M.A. Uymin, A.S. Minin, A.Y. Yermakov, A.V. Korolyov, M.Y. Balezin, S.Y. Sokovnin, A.S. Konev, S.F. Konev, L.S. Molochnikov, V.S. Gaviko, A.M. Demin, Magnetic properties and structure of TiO_2-Mn (0.73%) nanopowders: the effects of electron irradiation and vacuum annealing, Lett. Mater. 9 (2019) 91–96, https://doi.org/10.22226/2410-3535-2019-1-91-96.

[82] S. Alyatkin, I. Asharchuk, K. Khaydukov, A. Nechaev, O. Lebedev, Y. Vainer, V. Semchishen, E. Khaydukov, The influence of energy migration on luminescence kinetics parameters in upconversion nanoparticles, Nanotechnology 28 (2017) 035401, , https://doi.org/10.21883/OS.2019.01.47061.262-18.